Effects of Materials (Aluminum and Brass) and Bio-Inspired Trapezoidal Riblets on Mitigation of Erosion Induced by Cavitation Bubble Multiple Collapses

Ebrahim Kadivar *, Sasan Rezaee, Udo Löschner, Ould el Moctar

Posted Date: 19 June 2024

doi: 10.20944/preprints202406.1303.v1

Keywords: Cavitation; Erosion; Pure aluminum (1xxxAl or Al); Alpha brass (CuZn37 or CZ108); Bio-inspired sawtooth riblet

Article

Effects of Materials (Aluminum and Brass) and Bio-Inspired Trapezoidal Riblets on Mitigation of Erosion Induced by Cavitation Bubble Multiple Collapses

Ebrahim Kadivar [1,*], Sasan Rezaee [2], Udo Löschner [3] and Ould el Moctar [1]

[1] Institute of Ship Technology, Ocean Engineering and Transport Systems, University of Duisburg-Essen, Duisburg 47057, Germany
[2] Department of Physics and Energy Engineering, Amirkabir University of Technology, Tehran 159163-4311, Iran
[3] Laserinstitut Hochschule Mittweida, University of Applied Sciences Mittweida, Technikumplatz 17, 09648 Mittweida, Germany
* Correspondence: ebrahim.kadivar@uni-due.de; Tel.: +49-203-379-1173; Fax: +49-203-379-2779

Abstract: The current research investigates the effects of material and riblets on cavitation-induced erosion morphology, depth, and cross-sectional area through experimental approaches. To achieve these aims, the erosion of pure aluminum (1xxxAl or Al) and alpha brass (CuZn37 or CZ108) in the presence and absence of bio-inspired sawtooth riblets was examined after exposure to multiple collapses of single cavitation bubbles with a wall distance of 1.8. The results indicate that the erosion morphology resembles a rounded cone with a circular cross-section. Brass provides 21.6% more erosion resistance compared to Al in terms of material properties. Furthermore, the erosion for both Al (depth by 3.8% and width by 18.3%) and brass (depth by 7.9% and width by 27.4%) decreases in the presence of riblets compared to flat surfaces. The greater erosion resistance of brass compared to Al is attributed to the superior mechanical stability of brass, making it a potentially suitable alloy for propellers and hulls. In sum, the results reveal that riblet-provided materials with high mechanical durability are promising erosion-resistant materials for the shipping industry. However, the potential for chemical reactions in a cathodic environment should be addressed to provide a comprehensive perspective on reducing corrosion intensity.

Keywords: cavitation; erosion; pure aluminum (1xxxAl or Al); alpha brass (CuZn37 or CZ108); bio-inspired sawtooth riblet

1. Introduction

Cavitation is a phenomenon that usually occurs in ship and hydraulic machinery systems, in biochemical and biomedical and ultrasonic systems, and in various valves and injector nozzles, etc. Cavitation may cause mass loss, and it may damage the surface of immersed bodies of systems where cavitating flows or cavitation bubbles are generated. This cavitation-induced damage reduces the performance of such system [1–7]. The cavitation-induced damage is caused by the collapse of many tiny bubbles near a boundary. These tiny bubbles usually are of mesoscale, microscale, and nanoscale size. Previous research dealt mostly with the dynamics of a single cavitation bubble of mesoscale and microscale size near a boundary.

Pervious research numerically and experimentally studied the single cavitation bubble and its destructive effects near a solid boundary, such as erosion on the surface of the solid boundary [8–12]. The outcomes of these studies demonstrated that a microjet forms during the collapse process of the single cavitation bubble near a solid surface. This microjet, impacting on the solid boundary, induces

 doi:10.20944/preprints202406.1303.v1

surface erosion after several successive bubble collapses. Furthermore, a toroidal cavity structure forms after the first collapse, inducing more damage on the solid boundary. This toroidal cavity consists of several tiny bubbles that cause erosion after collapsing. Moreover, investigation the generation of acoustic transient laser-induced cavitation bubbles near solid boundaries revealed a significant pressure impact is generated inside a single cavitation bubble during its first collapse [13]. The impact on the solid surface reaches pressures up to 60×10^3 bar. They indicated that a major part of the bubble collapse energy is converted to acoustic energy.

Experimental studies on laser-induced cavitation bubbles collapsing near solid surfaces reveal that the collapse dynamics and direction of the bubble are influenced by the curvature of the solid surface and thermodynamic effects [14–18]. Additionally, the formation of counter jets and micro jets during the rebound process occurs at specific stand-off distances between the bubble center and the solid boundary, due to the pressure gradient around the single cavitation bubble. The morphology of the solid surface can also alter the momentum of the microjet formed during the bubble collapse process. In summary, these studies emphasize that if surfaces are provided with micro structured riblets, the cavitation-induced erosion from bubbles collapsing on solid boundaries can be mitigated.

Computational molecular dynamics (MD) simulations of the collapse dynamics of nanobubbles and their induced damage on solid boundaries provide valuable insights at the atomic and molecular scale regarding the mechanisms of collapse, erosion, and corrosion induced by cavitation [19–28]. The results revealed several key findings: the temperature of the nano jet rises sharply as the nanobubble shrinks after uniform compression [19,20]; the collapse time of the nanobubble is approximately in the picosecond range [21,22]; erosion on the solid surface is induced by the impact of nano jets molecules [23,24]; the induced shock wave cannot create holes or cavities in the absence of nanobubbles [25–27]; chemical reactions are accelerated during corrosion [21]; surface morphology significantly affects the momentum of the nano jet [28]; and nano riblets decrease the erosion induced by nano jets [29].

Summing up the literature review reveals that both experimental and computational results indicate that bubble collapse decreases bubble volume and forms a water jet that moves toward the solid surface. As a result of the impact between the water jet and the solid, the momentum of the water jet transfers to the solid, leading to erosion and corrosion. These undesirable outcomes, which reduce the lifetime of marine components, can be mitigated by riblets. However, it remains unclear how materials provided with riblets perform. Specifically, the effects of material surfaces provided with riblets on cavitation-induced erosion have not been fully addressed. In this context, the current study investigates the effects of pure aluminum (1xxxAl or 99%Al or Al) and alpha brass (CuZn37 or CZ108), both with and without bio-inspired sawtooth riblets, on cavitation-induced erosion morphology, depth, and cross-sectional area through experimental approaches. The results of this study not only reveal the effects of material on erosion but also disclose the impacts of riblets.

2. Background: Single Cavitation Bubble Near Solid Boundary

Formation of a bubble near the surface and its subsequent collapse can lead to erosion on the solid surface. To provide further insight into this phenomenon, Figure 1 illustrates the collapse of a bubble near the solid boundary surface, along with the solid boundary before, during, and after erosion. When a complete bubble with its maximum radius (R_{max}) forms near the flat rigid surface of the solid boundary (Figure 1a), the interaction between the boundary and the bubble's wall initiates the collapse process. At the onset of the collapse process, water vortices form and contribute to the shrinking and crumbling of the upper wall of the bubble (Figure 1b). As time elapses, additional water vortices are drawn into the vortices, contributing to the formation of a water jet (Figure 1c). The establishment of the water jet results in a reduction in the volume of the bubble.

As the water jet progresses forward, additional water vortices, formed due to the crumbling of the bubble wall, join the water jet and further reduce the remaining volume of the bubble. At this juncture, the water jet transforms into a water hammer and strikes the flat surface, resulting in surface erosion and the formation of a semi-spherical pit (Figure 1d). After erosion, the remaining water vortices form microbubbles (Figure 1e). Over time, the volume of microbubbles diminishes as a result

 doi:10.20944/preprints202406.1303.v1

of their rotation and interactions between the molecules on the microbubble wall and the molecules in the surrounding matrix. These processes decrease the radius of the microbubble, eventually generating nanobubbles (Figure 1f). Generally, nanobubbles persist within the matrix, capable of migrating freely. Upon collision with the flat surface, they contribute to nano-erosion.

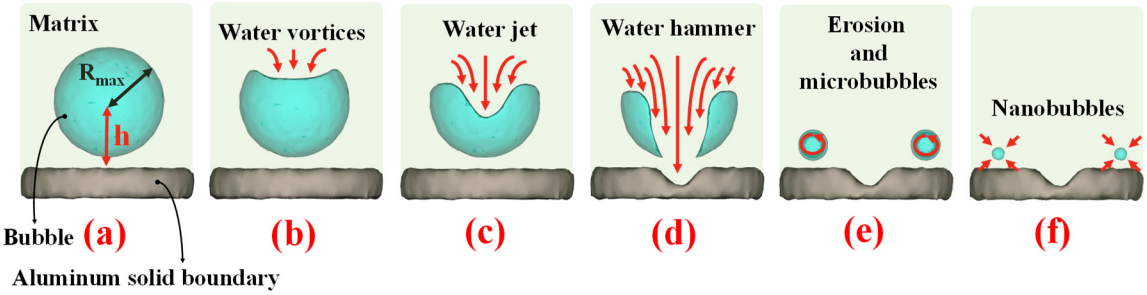

Figure 1. The schematic illustrates the single bubble collapse process near a flat solid boundary, depicting the maximum radius (R_{max}) of the bubble and the distance (h) between the center of the bubble and the surface of the solid boundary. (a) The complete single bubble near a flat solid boundary. (b) The collapse process initiates, and the upper wall of the bubble deteriorates more rapidly than the lower wall near the solid surface. This process attributes to the formation of water vortices. (c) The number of water vortices increases and converges into an arc shape, thereby decreasing the volume of the bubble. This phenomenon leads to the creation of a water jet. (d) The water jet forms and its volume increases as new water vortices are added, slicing through the volume of the bubble. Consequently, the water hammer is created and collides with the solid surface, resulting in erosion. (e) After erosion, the flow of water vortices leads to the creation of microbubbles. (f) The volume of the microbubble decreases and converts into nanobubbles. These nanobubbles can migrate through the matrix and collapse upon impact with the solid surface. Therefore, new nano erosion can occur.

In the case of riblets, different scenarios unfold. Riblets influence the flow of water vortices and consequently, the formation of the water jet and hammer. When the bubble collapses near a surface with riblets, the water vortices are diverted and separated. Consequently, the convergence of water vortices weakens, and they fail to merge into a cohesive water jet. Under these conditions, the resulting water jet is less powerful and lighter, leading to a weaker impact on the surface. Therefore, it can be inferred that erosion near surfaces with riblets may be reduced compared to those near flat surfaces. In this regard, an experimental approach is employed herein to elucidate the effects of riblets on induced erosion during bubble collapse.

3. Experimental Setup

3.1. Solid Boundary without and with Bio-Inspired Sawtooth Riblets

To reveal the effects of riblets and the material of the solid boundary on erosion, Al and brass (CuZn37 alloy; 63%Cu and 37%Zn) materials with and without riblets have been considered for cavitation testing. Figure 2 depicts the schematic of the shark-skin trapezoidal riblet pattern applied to the surfaces of Al and brass. As observed in this figure, the trapezoidal riblets are biologically inspired by shark-skin patterns (Figure 1a–c). The trapezoidal riblets provide hydrophobic characteristics [30] because the contact angle of a water droplet on the ribleted surface ranges between 90° and 180° (Figure 2d). In contrast, the flat surface without riblets is hydrophilic [30], with a contact angle between 0° and 90° (Figure 2d). Figure 2e,f demonstrate the flat surfaces of Al and brass without riblets, respectively. Conversely, Figure 2g,h show the surface morphology of Al and brass with riblets, respectively. Subsequently, these slabs were submerged in water, and bubbles created with a laser were used to perform erosion tests based on bubble collapse. More information concerning the geometry of riblets, the fingerprint of materials, and the physical parameters can be found in the relevant literature [17].

 doi:10.20944/preprints202406.1303.v1

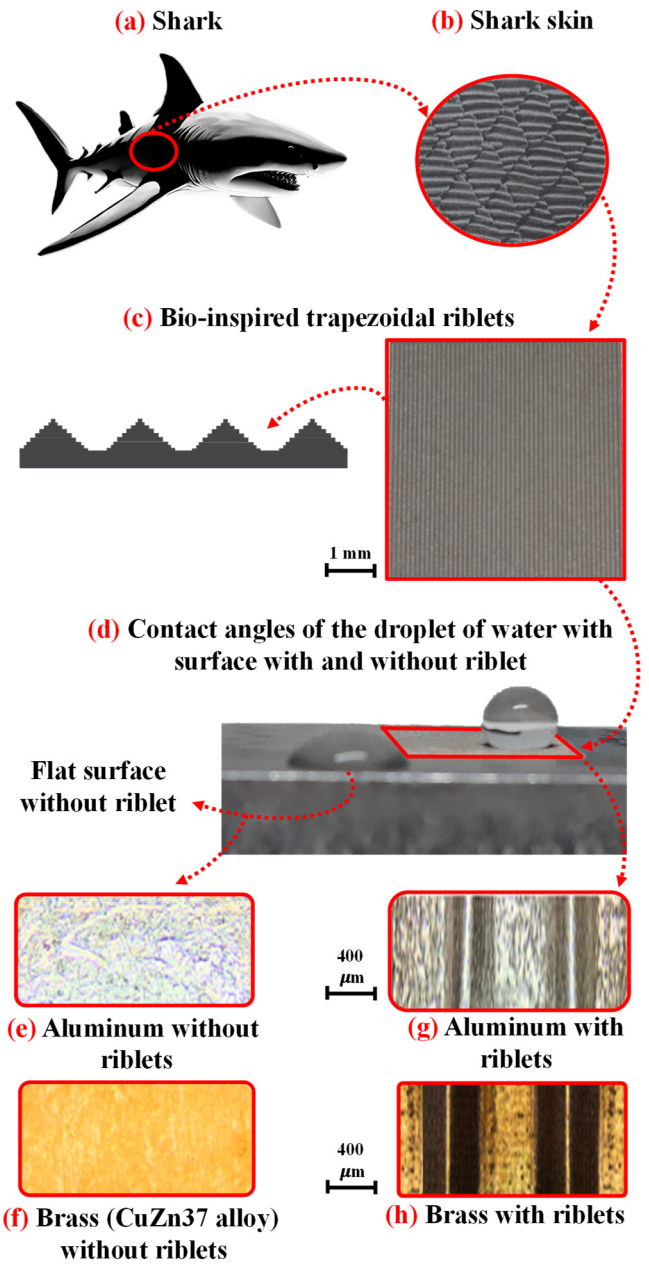

Figure 2. The application of the shark-skin trapezoidal riblet pattern to the surfaces of Al and brass (CuZn37 alloy; 63%Cu and 37%Zn). (a) An schematic of shark (to create this part, portrait of the shark was generated utilizing Adobe Firefly [31–33]), (b) Zoomed the shark-skin, (c) Designing bio-inspired trapezoidal riblets based on the shark-skin, (d) The contact angles of droplet of water with surface with and without riblet, (e) Aluminium surface without riblets, (f) Brass surface without riblet, (g) Aluminium surface with trapezoidal riblets, and (g) Brass surface with trapezoidal riblets.

3.2. Experimental Methodology

Figure 3a,b illustrate the arrangement of the experimental setup utilized to generate a single cavitation bubble near a rigid surface without and with riblets in separate experiments, respectively. The primary flow control in the cavitation experiment is achieved using a laser delay generator and a laser controller with an Q-switch Nd:YAG Litron laser. The laser beam is then deflected and focused by a deflector and lenses, respectively, inside a cuvette filled with water to create a single bubble. Finally, the bubble collapses, and the collapse dynamics are recorded using a high-speed camera and monitored by a computer. The wavelength and pulse duration of the laser are 1.064 nanometers (nm)

 doi:10.20944/preprints202406.1303.v1

and 4 nanoseconds (ns), respectively. Moreover, the laser produces a maximum output energy of 400 millijoules (mJ) and a maximum repetition rate of 10 hertz (Hz).

A single bubble with a R_{max} of approximately 1.5 millimeters (mm) and a standard spatial deviation of 14 micrometers (μm) can be generated with a laser beam energy level of approximately 14.6 mJ, obtained by using an adjustable laser controller. Inside the cuvette at the focal region of the lens, the energy and convergence of the laser beam generate high-temperature plasma close to the solid boundary. This causes the water in the plasma region to evaporate, leading to the creation of a single cavitation bubble with wall distance of γ=1.8. The growth and collapse processes of the bubble were recorded using a Phantom v9.1 high-speed camera with a sampling rate of 20 kHz and a resolution of 288×192 pixels. An internal high-speed controller and an external pulse/delay generator were coupled to trigger the camera with an exposure time of 10 μs.

After the growth of the bubble, its volume shrinks, and the collapse phenomenon occurs near the rigid surface due to the bubble-rigid surface interaction. The collapse process results in the formation of a water jet and hammer, which impact the rigid surface and lead to erosion. To obtain visible erosion, the cavitation-induced erosion generated by the collapse of the bubble was repeated five hundred times near the flat and ribleted surfaces. All experiments were performed at a temperature of 20 degrees Celsius and a pressure of 101 Kilopascals (kPa), which are well-known as atmospheric conditions. After performing all five hundred bubble collapses, the damage on the surfaces of Al and brass with and without riblets was analyzed using a confocal microscope. In this regard, a three-dimensional microscope maps of the damaged surface, optical microscope images, three-dimensional topographies of the damaged surface, and depth versus width diagrams were determined.

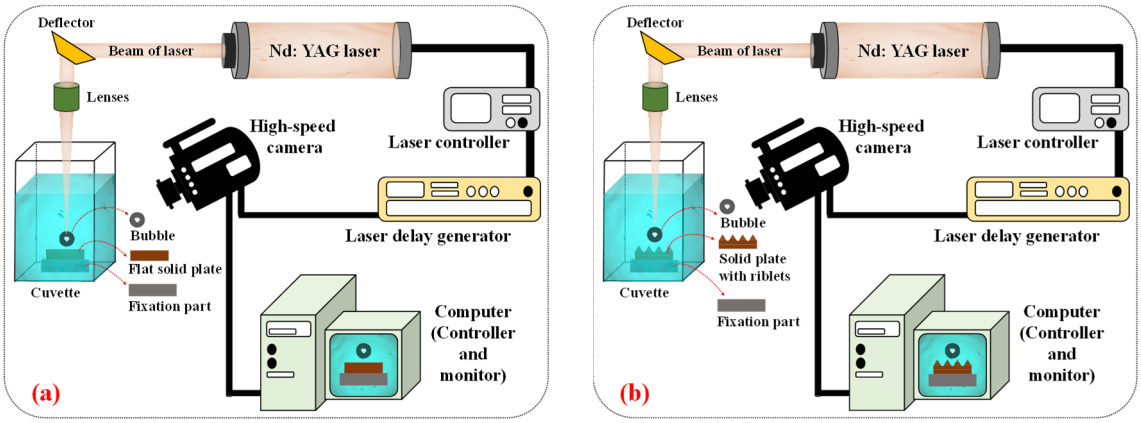

Figure 3. The arrangement of the experimental setup utilized to generate a single cavitation bubble near a rigid surface without and with riblets in separate experiments, respectively. (a) Experimental setup for flat surface, (b) Experimental setup for surface with riblets.

4. Results and Discussion

This section provides insight into erosion morphology, shape, and depth to reveal the influence of material and riblets on erosion and the intensity of the formed holes. The bubble collapse phenomena, which have been experimentally [17,18,34,35] and numerically [21,22,28,36] investigated in previous research by Kadivar and his team, are not addressed here; only the erosion and surface damage are examined. More details concerning bubble collapse dynamics can be found elsewhere. In this study, a three-dimensional map of the eroded surface and depth diagrams were obtained and plotted for Al and brass surfaces. To perform the cavitation test, 500 repeated single bubbles with a wall distance of γ = 1.8 were collapsed near the Al and brass surfaces. The eroded flat and ribleted surfaces were then captured for analysis. This strategy can disclose the effects of material and riblets on erosion intensity. More information concerning the effects of wall distance on erosion intensity can be found in Sagar [37] study. In relation to this report, the current research only considered a single relative wall distance equal to γ = 1.8.

 doi:10.20944/preprints202406.1303.v1

4.1. The Effects of the Material and Riblet on Cavitation-Induced Erosion Morphology

Figure 4 compares the captured optical microscope images, maps, and three-dimensional topographies of the damaged surfaces, which provided using a confocal microscope. This comparison provides the necessary analysis to disclose the effects of material and surface morphology on cavitation-induced erosion caused by multiple single bubble collapses. Figure 4 shows the relevant microscope images of the eroded surfaces of Al and brass side by side to provide sufficient conditions for comparing erosion intensity. The color map depicted on the right of this figure shows the color contours for the maps and three-dimensional topographies of the damaged surfaces, which can be observed in Figure 4c–f,i–l. The optical microscope images were also indicated in Figure 4a,b,g–h.

Figure 4a,b show the optical microscope images of the eroded Al and brass surfaces without riblets, respectively. Based on these photos, it can be concluded that the cavitation-induced damage shape caused by bubble collapse resembles a rounded cone. Generally, the cross-section of erosion is circular because the water hammer front wave, formed subsequent to the water jet and complete collapse of the bubble, provides a semi-spherical shape, and its two-dimensional map is circular on surface. Therefore, the initial eroded area mimics a circular shape. More information regarding water hammer formation subsequent to the water jet and complete collapse of the bubble can be found in detail elsewhere [9,17,22,28]. This research focuses only on the damage caused by the water hammer on the surface. Creating a single bubble at the same position and repeatedly collapsing it leads to erosion growth in depth, ultimately resulting in an erosion shape that mimics a rounded cone with a circular cross-section.

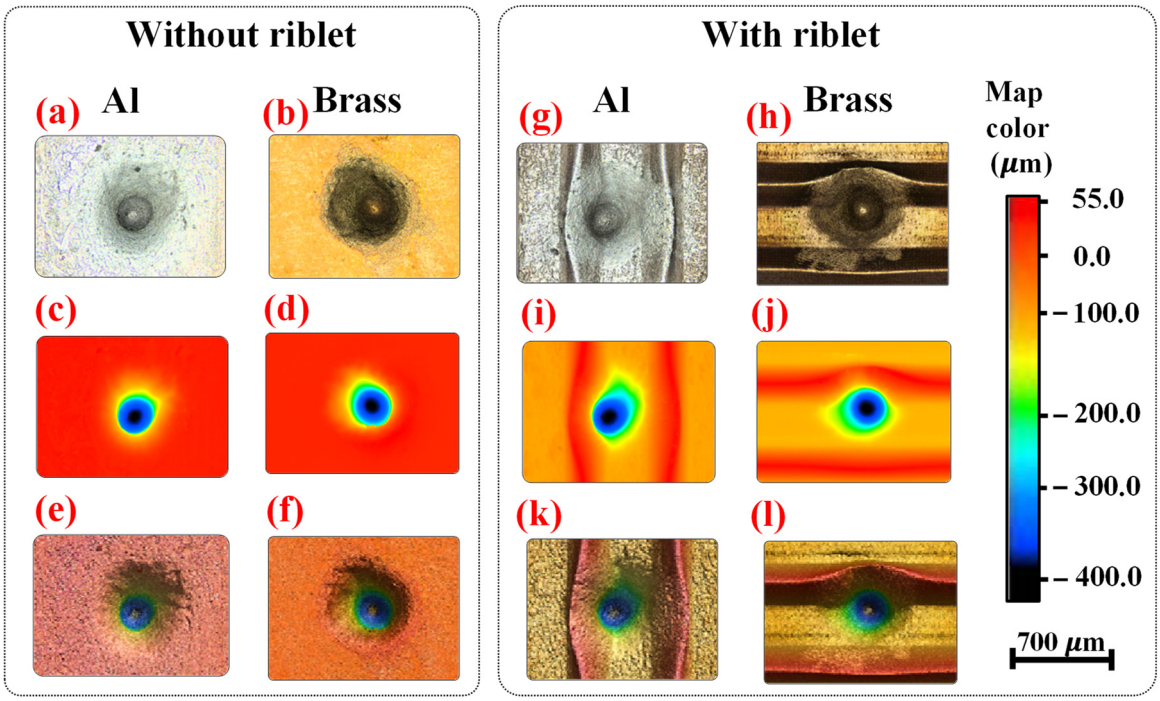

Figure 4. Microscope images of Al and brass surface without and with riblets after 500 single cavitation bubble with wall distance of γ=1.8. (a) and (g) show the optical microscope image of damaged Al surface without and with riblet, respectively. (b) and (h) illustrate the optical microscope image of damaged brass surface without and with riblet, respectively. (c) and (i) indicate map of the damaged Al surface without and with riblet, respectively. (d) and (j) represent map of the damaged brass surface without and with riblet, respectively. (e) and (k) depict three-dimensional topography of damaged Al surface without and with riblet, respectively. (f) and (l) demonstrate three-dimensional topography of damaged brass surface without and with riblet, respectively. All experiments (cavitation bubble) were performed at a temperature of 20 degrees Celsius and a pressure of 101 kilopascals (kPa), which are well-known as atmospheric conditions.

 doi:10.20944/preprints202406.1303.v1

The intercomparison of erosion shapes for Al and brass with riblets in Figure 4g and 4h, respectively, reveals similar erosion morphology to surfaces without riblets. However, the erosion occurs between two riblet lines due to the initial experimental setup, and it seems that the erosion area and depth are decreased in comparison to flat surfaces. The similar shape of erosion originates from the similar collapse characteristics of the water hammer and jet in the presence and absence of riblets. Because the bubble collapse dynamics, formed water jet, and water hammer near the flat and ribleted surfaces are similar, the erosion shapes on flat and ribleted surfaces resemble rounded cones with circular cross-sections. In contrast, the lower erosion depth and area on ribleted surfaces result from the effects of riblets on bubble collapse time and the momentum of the water hammer and jet. Riblets can decrease the bubble collapse time and reduce the momentum carried by the water jet and hammer [9,17,29], resulting in lower erosion depth and area.

Maps of the damaged surfaces without riblets for Al and brass are depicted in Figure 4c,d to provide more evidence of erosion morphology and depth. Based on these figures, the erosion area can be divided into five regions. The first region, with a semi-circular shape, which is well-known as the cross-section of a cone, shows a depth between 0 to 100 μm. The second region, with a lower cross-sectional area and yellow color, indicates a depth of approximately 150 μm. The third and fourth regions, with green and blue colors, correspond to depths of 200 μm and 300 μm, respectively. Finally, the fifth region, with a navy blue color and depth of 330-450 μm, discloses the approximate depth of erosion. In the case of Al and brass with riblets, as shown in Figure 4i,j, it is clear that the morphology of erosion is similar to that of flat surfaces. However, in the fifth region, the depth of erosion decreases to 315-416 μm.

Figure 4e,f compare the three-dimensional topography of the damaged Al and brass surfaces without riblets, respectively. These figures show that the final depth of erosion for flat Al and brass surfaces, indicated by the navy blue color, is approximately 330-450 μm. In contrast, for the ribleted surfaces of Al and brass shown in Figure 4k and 4l, respectively, the final depth of erosion is in the range of 315-316 μm, also indicated by the navy blue color. An intercomparison of the final erosion depth between Al and brass surfaces with and without riblets reveals that the erosion depth decreases in the presence of riblets. This is because riblets can decrease the momentum of the water hammer formed toward the surface following bubble collapse by causing the separation of water vortices formed during the collapse. Consequently, the impulse of the water hammer decreases, reducing erosion.

In summary, it is clear that erosion depth decreases in the presence of riblets because riblets can separate the water vortices, thereby decreasing the impulse of the water hammer. Moreover, the erosion morphology reveals a rounded cone with a circular cross-section. Furthermore, the circular cross-sectional area and depth of erosion decrease and increase, respectively, along the axis of the cone. The circular cross-sectional area is formed due to the two-dimensional impulse map of the water hammer. The decrease in the circular area of the cross-section along the axis of the cone is due to the increasing wall distance of the bubble as the depth of the eroded region grows after repeated collapses. For several initial bubble collapses, the fresh surface stands against the water hammer, and the maximum concentration of the water hammer impact on the surface leads to large erosion with a circular shape. However, as erosion occurs and grows with repeated collapses, the distance between the depth of erosion and the center of the bubble increases, leading to a rise in wall distance and reducing the impulse of the water hammer on the surface. In this case, only the front part of the water hammer impacts the surface, resulting in a smaller circular cross-sectional erosion with a circular shape. On the other hand, repeated bubble collapses lead to continuous impulse and increase the erosion depth along the cone axis.

4.2. The Effects of the Material and Riblet on Cavitation-Induced Erosion Depth and Cross-Section

The previous section provides precise information concerning the effects of material and riblets on cavitation-induced erosion morphology; however, the exact amount of cross-sectional area of erosion remains unclear, and the depth of erosion is expressed within the range of 330-450 μm and 315-316 μm for flat and ribleted surfaces, respectively. In this regard, this section offers a three-

Preprints.org (www.preprints.org) | NOT PEER-REVIEWED | Posted: 19 June 2024 doi:10.20944/preprints202406.1303.v1

dimensional map of the eroded surface and a diagram of depth to disclose the exact amount of cross-sectional area and depth of erosion, as shown in Figure 5. This figure presents the three-dimensional map of the eroded surface, a diagram of depth versus width of the damaged surface along the horizontal line, and a diagram of depth versus width of the damaged surface along the vertical line induced by 500 single cavitation bubbles with a wall distance of γ = 1.8 in parts I, II, and III, respectively.

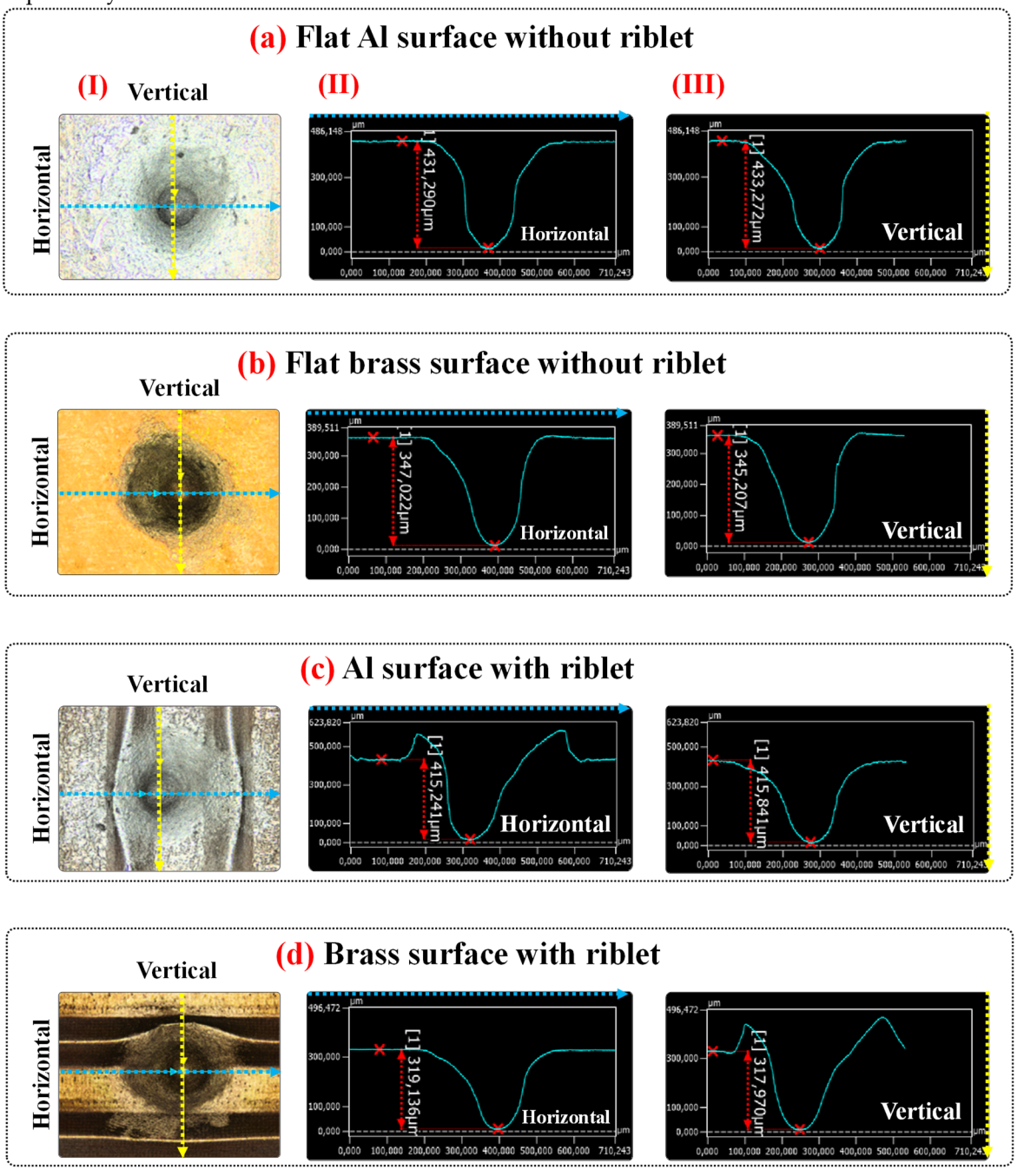

Figure 5. Three dimensional map of the eroded surface and diagram of depth. (I) Three dimensional map of the damaged surface, (II) diagram of depth versus width of the damaged surface along horizontal line, and (III) diagram of depth versus width of the damaged surface along vertical line induced by 500 single cavitation bubble with wall distance of γ=1.8. (a) Flat Al surface without riblet, (b) Flat brass surface without riblet, (c) Al surface with riblet, and (d) brass surface with riblet. All experiments (cavitation bubble) were performed at a temperature of 20 degrees Celsius and a pressure of 101 kilopascals (kPa), which are well-known as atmospheric conditions.

 doi:10.20944/preprints202406.1303.v1

Figure 5a illustrates the average depth of erosion of 432.281 μm and an average radius of the cross-section of erosion of 162.5 μm for Al with a flat surface. Intercomparison of these values with the average depth (346.115 μm) and radius (157.5 μm) of the cross-section of erosion for brass with a flat surface in Figure 5b reveals that both the depth and area of erosion in brass are smaller than those in Al by 19.9% and 3.0%, respectively. These results originate from the nature of the physical properties of Al and brass. Brass exhibits a Young's modulus of 97 Gigapascals (GPa), a shear modulus of 37 GPa, and a Poisson's ratio of 0.34 (dimensionless) [38]. In comparison, Al has a Young's modulus of 68 GPa, a shear modulus of 25 GPa, and a Poisson's ratio of 0.33 [38]. Intercomparison of these values proves that brass offers greater mechanical stability than Al, thereby being able to tolerate the impulse of the water hammer more effectively than Al and resulting in lower erosion depth and area in comparison to Al.

Based on the obtained results for the exact amount of cross-sectional area and depth of erosion in the case of Al and brass with flat surface morphology, it can be expected that in the presence of riblets, the erosion area and depth for brass will be lower than for Al. Intercomparison of the average depth and radius of the cross-section of erosion for Al and brass with riblets in Figure 5c and 5d, respectively, confirms this prediction. According to these figures, the average depth of erosion for Al and brass with riblets are 415.541 and 318.553 μm, respectively. These outcomes clearly indicate that brass with riblets exhibits 23.3% less erosion compared to Al with riblets. Moreover, in the presence of riblets, the erosion depth of Al and brass is reduced by 3.8% and 7.9%, respectively, in comparison with flat surfaces. Furthermore, the erosion depth of brass is lower than that of Al when both have surfaces with riblets.

Intercomparison of erosion width along horizontal and vertical axes for surfaces with and without riblets in Figure 5 indicates that the width of erosion perpendicular to riblet lines decreases, while this value parallel to riblet lines remains similar to those observed for flat surfaces. The widths of erosion parallel to riblet lines are 350 μm and 322 μm for Al and brass with riblets, respectively. Comparing these values with the width of erosion for Al (350 μm) and brass (320 μm) without riblets shows that riblets along their lines do not affect water vortices and thereby do not decrease erosion width. On the other hand, a completely different results are observed perpendicular to the riblet lines. It is evident that the width of erosion perpendicular to riblet lines for Al and brass with riblets are 245 μm and 225 μm, respectively. Intercomparison of these results with the values for Al (300 μm) and brass (310 μm) without riblets signifies that the presence of riblets reduces the width of erosion by 18.3% and 27.4% for Al and brass, respectively. This outcome is attributed to the riblets, as perpendicular to riblet lines the water vortices separate, and the impulse of the water hammer decreases along this axis, thereby reducing the width of erosion.

This section outlines the significant effects of material type and riblets on erosion. Brass exhibits 21.6% greater erosion resistance compared to Al due to its mechanical stability. In other words, brass experiences less erosion than Al because of its inherent physical properties. Riblets reduce the depth and width of erosion by 3.8% and 18.3%, respectively, for Al. In the case of brass, riblets decrease the depth and width of erosion by 7.9% and 27.4%, respectively. The width of erosion perpendicular to riblet lines decreases more than parallel to riblet lines due to the separation effects of water vortices. Therefore, it can be concluded that riblets can provide anti-erosion properties for materials against fluid and cavitation damage.

5. Outlook and Perspective

In this research, the influence of materials (Al and brass) and bio-inspired sawtooth riblets on cavitation-induced erosion morphology, depth, and cross-sectional area has been investigated using experimental approaches. The main findings of this study reveal that erosion depth and cross-sectional area are reduced due to the effects of bio-inspired sawtooth riblets. Additionally, brass demonstrates greater erosion resistance compared to Al, with a 7.9% reduction in depth and a 27.4% reduction in erosion width, compared to a 3.8% reduction in depth and an 18.3% reduction in erosion width for Al. This is attributed to the greater mechanical stability of brass. Moreover, results show that the width of erosion perpendicular to riblet lines decreases more than parallel to riblet lines.

 doi:10.20944/preprints202406.1303.v1

These findings are attributed to the physical properties of the materials and the passive erosion control method provided by riblets. However, in seawater, which represents the primary application of anti-erosion materials for ship and submarine propellers and hulls, materials are exposed to a cathodic environment that leads to corrosion [39–41]. Therefore, it is necessary to determine the behavior of riblet direction and the impact of the cathodic environment in propellers and hulls.

5.1. Riblets Morphology

In the case of riblets morphology, the geometry and pattern of riblets can significantly influence the degree of erosion reduction. The height of riblets, the angles of the V-shaped sawtooth, and the distance between riblet lines should be designed considering the most probable bubbles near propellers and hulls. Bubbles of different radii can produce various water jets and hammers, resulting in different impulses and erosions. Each water hammer, depending on its volume and momentum, causes a specific impulse and erosion pattern. At the interface between propellers (or hulls) and seawater, different riblet geometries lead to varying effects on the separation of water vortices, thus affecting erosion reduction. Therefore, the morphology of riblets should be designed considering the most probable bubble characteristics to offer high erosion resistance.

The orientation pattern of riblet lines is another geometric factor that can be useful in reducing erosion. The results obtained in the current study indicate that the width of erosion perpendicular to riblet lines decreases more than parallel to riblet lines, as illustrated in Figure 6a. It can be predicted that if a netted pattern is considered for riblets, the erosion width could be limited in both perpendicular and parallel directions. The schematic of the netted pattern is depicted in Figure 6b–d. It is worth mentioning that in a netted pattern, the height, angles, and size of netted cells must be designed with regard to the most probable bubbles near propellers and hulls to offer maximum erosion resistance. These patterns can be applied to the surface of the material using micro [42] and electron beam drilling [43] techniques. Evidence of the positive effects of netted pattern riblets on erosion reduction can be investigated through molecular dynamics and finite element methods initially. Subsequently, experimental approaches can be utilized. This strategy not only can be useful to prove the effects of the netted pattern riblets on erosion resistance but also decrease the cost of research validation.

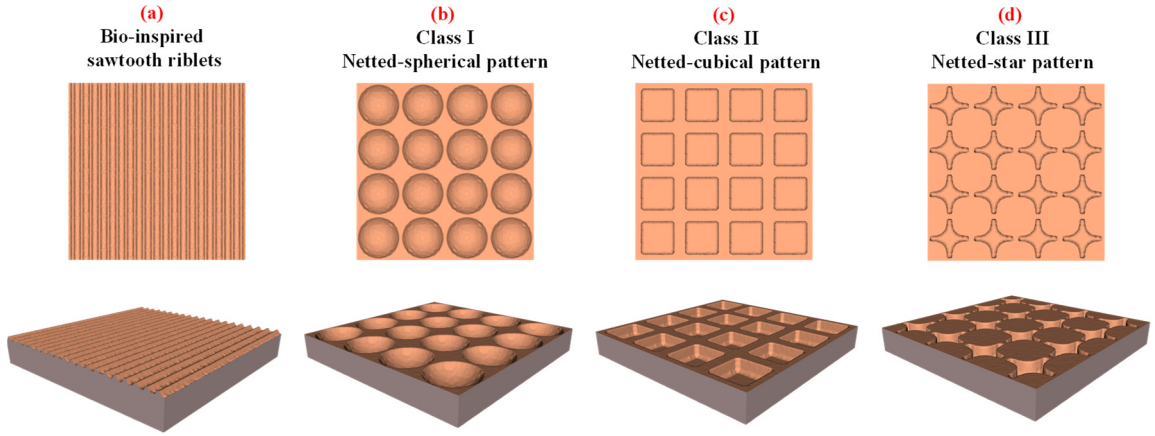

Figure 6. Intercomparison of the bio-inspired sawtooth and proposed riblets. (a) Bio-inspired sawtooth riblets. (b) Proposed class I riblets (netted-spherical pattern). (c) Proposed class II riblets (netted-cubical pattern). (d) Proposed class III riblets (netted-star pattern).

5.2. The Effects of the Cathodic Environment

In seawater, propellers and hulls are submerged in a cathodic environment where chemical reactions and erosion occur simultaneously [39–41], a process known as corrosion. This study investigated the effects of material and riblets on erosion; however, the effects of chemical reactions were not addressed. Therefore, it is necessary to consider the probable chemical reactions, which

 doi:10.20944/preprints202406.1303.v1

significantly depend on the materials, as an influencing parameter in corrosion. Investigation of corrosion can be performed using cost-effective reactive molecular dynamics (reactive-MD) [21] and density functional theory (DFT) [44] methods, as well as experimental methods [45]. These techniques can successfully reveal the probable chemical reactions. For example, regarding the reaction of Al [21] and brass (Cu-20Zn) [45] with pure water, the following equation can be expected.

For Al: $2Al(s) + H_2O(l) \rightarrow AlOH(s) + AlH(s)$ (1)

For Brass: $Brass(Cu\text{-}20Zn)(s) + 2H_2O\ (l) \rightarrow Cu_2O(s) + ZnO(s) + 2H_2(g)$ (2)

Here, s denotes the solid, l signifies the liquid, and g depicts the gas phases. H_2O, AlOH, and AlH are water, aluminum monohydroxide, and aluminum monohydride, respectively. Cu_2O is cuprous oxide, ZnO represents zinc oxide, and H_2 points to the hydrogen gas. Based on Eqs. (1) and (2), it is evident that Al and brass can corrode when they come into contact with pure water. Similarly, chemical reactions occur under cathodic environments, producing chemical products and decreasing the lifetime of materials. Therefore, the corrosion process (erosion + chemical reaction) under cathodic environments should be addressed for Al and brass to provide a comprehensive overview of the sufficiency of these materials for corrosion resistance.

6. Conclusions

Erosion of propellers and hulls is a critical issue in the shipping industry, significantly reducing the lifespan of components in seawater. Offering erosion-resistant materials to control and reduce erosion can increase the lifespan of these components and lower repair and maintenance costs. In this regard, the effects of materials (Al and brass) and bio-inspired sawtooth riblets on cavitation-induced erosion morphology, depth, and cross-sectional area have been probed through experimental methods to provide scientific and comparable insights into erosion. These aims were achieved by subjecting Al and brass surfaces, both with and without riblets, to 500 single cavitation bubbles with a wall distance of γ=1.8, followed by capturing optical microscopy images and depth diagrams of erosion.

The results indicate that for both Al and brass with flat and ribleted surfaces, the erosion morphology resembles a rounded cone with a circular cross-section. However, the height of the cone axis (erosion depth) and the cross-sectional area of the erosion depend on the material and the presence of riblets. Initially, erosion begins with a large circular cross-sectional area, and as the depth of erosion increases, the cross-sectional radius decreases. In other words, the increasing depth of erosion along the cone axis results from multiple bubble collapses and the subsequent multiple impulses of water hammers. This process decreases the cross-sectional area of erosion due to the increasing wall distance of the bubble as the depth of the eroded region grows after repeated collapses.

In terms of material properties, brass provides 21.6% more erosion resistance compared to Al due to its mechanical stability. Regarding riblets, Al with riblets reduces the depth and width of erosion by 3.8% and 18.3%, respectively, compared to Al with a flat surface. In contrast, brass with riblets decreases the depth of erosion by 7.9% and the width by 27.4% compared to brass without riblets. Concerning riblet geometry, the width of erosion perpendicular to riblet lines decreases more than parallel to riblet lines due to the separation effects of water vortices. The summary of results reveals that materials with durable mechanical stability, when provided with riblets, can significantly decrease erosion. However, the probability of chemical reactions in a cathodic environment and the exploration of other potential riblet patterns should be examined to provide a comprehensive viewpoint on corrosion and to achieve maximum erosion intensity reduction.

References

1. E. Kadivar, T. Ochiai, Y. Iga, O. el Moctar, An experimental investigation of transient cavitation control on a hydrofoil using hemispherical vortex generators, J. Hydrodyn. 33 (2021) 1139–1147. https://doi.org/10.1007/s42241-021-0097-6.

2. E. Kadivar, M. V. Timoshevskiy, M.Y. Nichik, O. El Moctar, T.E. Schellin, K.S. Pervunin, Control of unsteady partial cavitation and cloud cavitation in marine engineering and hydraulic systems, Phys. Fluids. 32 (2020). https://doi.org/10.1063/5.0006560.
3. R. Fortes Patella, T. Choffat, J.L. Reboud, A. Archer, Mass loss simulation in cavitation erosion: Fatigue criterion approach, Wear. 300 (2013) 205–215. https://doi.org/10.1016/j.wear.2013.01.118.
4. M. Sadri, E. Kadivar, Numerical investigation of the cavitating flow and the cavitation-induced noise around one and two circular cylinders, Ocean Eng. 277 (2023) 114178. https://doi.org/10.1016/j.oceaneng.2023.114178.
5. M. Dular, B. Bachert, B. Stoffel, B. Širok, Relationship between cavitation structures and cavitation damage, Wear. 257 (2004) 1176–1184. https://doi.org/10.1016/j.wear.2004.08.004.
6. G.E. Reisman, Y.C. Wang, C.E. Brennen, Observations of shock waves in cloud cavitation, J. Fluid Mech. 355 (1998) 255–283. https://doi.org/10.1017/S0022112097007830.
7. Y. Lin, E. Kadivar, O. El Moctar, J. Neugebauer, T.E. Schellin, Experimental investigation on the effect of fluid-structure interaction on unsteady cavitating flows around flexible and stiff hydrofoils, Phys. Fluids. 34 (2022). https://doi.org/10.1063/5.0099776.
8. T. Wei, C.R. Smith, Secondary vortices in the wake of circular cylinders, J. Fluid Mech. 169 (1986) 513–533. https://doi.org/10.1017/S0022112086000733.
9. E. Kadivar, O. el Moctar, H.J. Sagar, Experimental study of the influence of mesoscale surface structuring on single bubble dynamics, Ocean Eng. 260 (2022) 111892. https://doi.org/10.1016/j.oceaneng.2022.111892.
10. A. Philipp, W. Lauterborn, Cavitation erosion by single laser-produced bubbles, J. Fluid Mech. 361 (1998) 75–116. https://doi.org/10.1017/S0022112098008738.
11. Y. Tomita, A. Shima, Mechanisms of impulsive pressure generation and damage pit formation by bubble collapse, J. Fluid Mech. 169 (1986) 535–564. https://doi.org/10.1017/S0022112086000745.
12. W. Lauterborn, H. Bolle, Experimental investigations of cavitation-bubble collapse in the neighbourhood of a solid boundary, J. Fluid Mech. 72 (1975) 391–399. https://doi.org/10.1017/S0022112075003448.
13. A. Vogeland, W. Lauterborn, Acoustic transient generation by laser-produced cavitation bubbles near solid boundaries, J. Acoust. Soc. Am. 84 (1988) 719–731. https://doi.org/10.1121/1.396852.
14. O. Lindau, W. Lauterborn, Cinematographic observation of the collapse and rebound of a laser-produced cavitation bubble near a wall, J. Fluid Mech. 479 (2003) 327–348. https://doi.org/10.1017/S0022112002003695.
15. Y. Tomita, P.B. Robinson, R.P. Tong, J.R. Blake, Growth and collapse of cavitation bubbles near a curved rigid boundary, J. Fluid Mech. 466 (2002) 259–283. https://doi.org/10.1017/S0022112002001209.
16. M. Dular, T. Požar, J. Zevnik, R. Petkovšek, High speed observation of damage created by a collapse of a single cavitation bubble, Wear. 418–419 (2019) 13–23. https://doi.org/10.1016/j.wear.2018.11.004.
17. E. Kadivar, O. el Moctar, R. Skoda, U. Löschner, Experimental study of the control of cavitation-induced erosion created by collapse of single bubbles using a micro structured riblet, Wear. 486–487 (2021) 204087. https://doi.org/10.1016/j.wear.2021.204087.
18. T.H. Phan, E. Kadivar, V.T. Nguyen, O. El Moctar, W.G. Park, Thermodynamic effects on single cavitation bubble dynamics under various ambient temperature conditions, Phys. Fluids. 34 (2022) 23318. https://doi.org/10.1063/5.0076913.
19. Y. Murai, Y. Matsumoto, Numerical study of the three-dimensional structure of a bubble plume, J. Fluids Eng. Trans. ASME. 122 (2000) 754–760. https://doi.org/10.1115/1.1313245.
20. C. Xiao, D.M. Heyes, J.G. Powles, The collapsing bubble in a liquid by molecular dynamics simulations, Mol. Phys. 100 (2002) 3451–3468. https://doi.org/10.1080/0026897021000016710.
21. M. Ghoohestani, S. Rezaee, E. Kadivar, M.A. Esmaeilbeig, Reactive-dynamic characteristics of a nanobubble collapse near a solid boundary using molecular dynamic simulation, Phys. Fluids. 35 (2023). https://doi.org/10.1063/5.0139169.
22. M. Ghoohestani, S. Rezaee, E. Kadivar, O. el Moctar, Thermodynamic effects on nanobubble's collapse-induced erosion using molecular dynamic simulation, Phys. Fluids. 35 (2023). https://doi.org/10.1063/5.0154822.
23. Z. Gao, W. Wu, W. Sun, B. Wang, Understanding the Stabilization of a Bulk Nanobubble: A Molecular Dynamics Analysis, Langmuir. 37 (2021) 11281–11291. https://doi.org/10.1021/acs.langmuir.1c01796.
24. D. Sun, X. Lin, Z. Zhang, N. Gu, Impact of Shock-Induced Lipid Nanobubble Collapse on a Phospholipid Membrane, J. Phys. Chem. C. 120 (2016) 18803–18810. https://doi.org/10.1021/acs.jpcc.6b04086.
25. N. Nan, D. Si, G. Hu, Nanoscale cavitation in perforation of cellular membrane by shock-wave induced nanobubble collapse, J. Chem. Phys. 149 (2018). https://doi.org/10.1063/1.5037643.
26. K.P. Santo, M.L. Berkowitz, Shock Wave Induced Collapse of Arrays of Nanobubbles Located Next to a Lipid Membrane: Coarse-Grained Computer Simulations, J. Phys. Chem. B. 119 (2015) 8879–8889. https://doi.org/10.1021/jp505720d.
27. U. Adhikari, A. Goliaei, M.L. Berkowitz, Mechanism of membrane poration by shock wave induced nanobubble collapse: a molecular dynamics study, J. Phys. Chem. B. 119 (2015) 6225–6234. https://doi.org/10.1021/acs.jpcb.5b02218.

 doi:10.20944/preprints202406.1303.v1

28. S. Rezaee, E. Kadivar, O. el Moctar, Molecular dynamics simulations of a nanobubble's collapse-induced erosion on nickel boundary and porous nickel foam boundary, J. Mol. Liq. 397 (2024) 124029. https://doi.org/10.1016/j.molliq.2024.124029.
29. S. Rezaee, E. Kadivar, O. el Moctar, The role of sawtooth-shaped nano riblets on nanobubble dynamics and collapse-induced erosion near solid boundary, J. Mol. Liq. 405 (2024) 124947. https://doi.org/10.1016/j.molliq.2024.124947.
30. A.E. Pap, C. Dücso, K. Kamaras, G. Battistig, I. Bársony, Heavy water in gate stack processing, in: Mater. Sci. Forum, Trans Tech Publ, 2008: pp. 119–131. https://doi.org/10.4028/www.scientific.net/msf.573-574.119.
31. J. Hutson, J. Lively, B. Robertson, P. Cotroneo, M. Lang, Expanding Horizons: AI Tools and Workflows in Art Practice, in: Springer Ser. Cult. Comput., Springer, 2024: pp. 101–132. https://doi.org/10.1007/978-3-031-45127-0_5.
32. D.C. Epstein, I. Jain, O. Wang, R. Zhang, Online detection of ai-generated images, in: Proc. IEEE/CVF Int. Conf. Comput. Vis., 2023: pp. 382–392.
33. M. Healy, Approaches to Generative Artificial Intelligence, A Social Justice Perspective, SSRN Electron. J. (2023). https://doi.org/10.2139/ssrn.4544617.
34. H.J. Sagar, O. el Moctar, Dynamics of a cavitation bubble near a solid surface and the induced damage, J. Fluids Struct. 92 (2020) 102799. https://doi.org/10.1016/j.jfluidstructs.2019.102799.
35. E. Kadivar, T.H. Phan, W.G. Park, O. El Moctar, Dynamics of a single cavitation bubble near a cylindrical rod, Phys. Fluids. 33 (2021). https://doi.org/10.1063/5.0070847.
36. E. Kadivar, A. Rajabpour, O. El Moctar, Nanobubble Collapse Induced Erosion near Flexible and Rigid Boundaries: A Molecular Dynamics Study, Fluids. 8 (2023) 154. https://doi.org/10.3390/fluids8050154.
37. H.J. Sagar, Numerical and Experimental Investigation of Laser-Induced Cavitation Bubbles and Induced Damage, (2018) 430–439.
38. NOOR HUSSEIN, Materials Science and Engineering, CreateSpace Independent Publishing Platform, 2017.
39. Y. Xu, Q. Zhang, Q. Zhou, S. Gao, B. Wang, X. Wang, Y. Huang, Flow accelerated corrosion and erosion–corrosion behavior of marine carbon steel in natural seawater, Npj Mater. Degrad. 5 (2021) 56. https://doi.org/10.1038/s41529-021-00205-1.
40. C. Googan, Marine Corrosion and Cathodic Protection, CRC Press, 2022. https://doi.org/10.1201/9781003216070.
41. Y. Yan, H. Zhu, Z. Fan, J. Zhao, S. Jiang, Corrosion Behavior of Reinforcing Steel in the Immersed Tube Tunnel (ITT) under Submarine Environment, Materials (Basel). 16 (2023) 3300. https://doi.org/10.3390/ma16093300.
42. M. Hasan, J. Zhao, Z. Jiang, A review of modern advancements in micro drilling techniques, J. Manuf. Process. 29 (2017) 343–375. https://doi.org/10.1016/j.jmapro.2017.08.006.
43. D.G. Howitt, S.J. Chen, B.C. Gierhart, R.L. Smith, S.D. Collins, The electron beam hole drilling of silicon nitride thin films, J. Appl. Phys. 103 (2008). https://doi.org/10.1063/1.2828157.
44. P.A. Johnson, L.J. Bartolotti, P.W. Ayers, T. Fievez, P. Geerlings, Charge density and chemical reactions: A unified view from conceptual DFT, in: Mod. Charg. Anal., Springer, 2012: pp. 715–764. https://doi.org/10.1007/978-90-481-3836-4_21.
45. P. Qiu, C. Leygraf, Initial oxidation of brass induced by humidified air, Appl. Surf. Sci. 258 (2011) 1235–1241. https://doi.org/10.1016/j.apsusc.2011.09.080.